Fuel 157 (2015) 140–150

Contents lists available at ScienceDirect

Fuel

journal homepage: www.elsevier.com/locate/fuel

Microscopic imaging of the initial stage of diesel spray formation

Cyril Crua [a,*], Morgan R. Heikal [a], Martin R. Gold [b]

[a] Centre for Automotive Engineering, University of Brighton, Brighton BN2 4GJ, UK
[b] BP Formulated Products Technology, Pangbourne, UK

HIGHLIGHTS

- We captured microscopic images of diesel, kerosene and RME at diesel engine conditions.
- The fluid exits the nozzle with a mushroom-like structures that propels a ligament.
- We propose that fuel can remain trapped in the injector holes after injection.
- We showed this mechanism occurs under typical diesel engine conditions.

ARTICLE INFO

Article history:
Received 27 February 2015
Received in revised form 14 April 2015
Accepted 16 April 2015
Available online 7 May 2015

Keywords:
Diesel sprays
Microscopy
Ultra-fast framing video

ABSTRACT

Detailed measurements of near-nozzle spray formation are essential to better understand and predict the physical processes involved in diesel fuel atomisation. We used long-range microscopy to investigate the primary atomisation of diesel, biodiesel and kerosene fuels in the near-nozzle region, both at atmospheric and realistic engine conditions. High spatial and temporal resolutions allowed a detailed observation of the very emergence of fuel from the nozzle orifice. The fluid that first exited the nozzle resembled mushroom-like structures, as occasionally reported by other researchers for atmospheric conditions, with evidence of interfacial shearing instabilities and stagnation points. We captured the dynamics of this phenomenon using an ultra-fast framing camera with frame rates up to 5 million images per second, and identified these structures as residual fluid trapped in the orifice between injections. The residual fluid has an internal vortex ring motion which results in a slipstream effect that can propel a microscopic ligament of liquid fuel ahead. We showed that this mechanism is not limited to laboratory setups, and that it occurs for diesel fuels injected at engine-like conditions with production injectors. Our findings confirm that fuel can remain trapped in the injector holes after the end of injection. Although we could not measure the hydrocarbon content of the trapped vapourised fluid, we observed that its density was lower than that of the liquid fuel, but higher than that of the in-cylinder gas. We conclude that high-fidelity numerical models should not assume in their initial conditions that the sac and orifices of fuel injectors are filled with in-cylinder gas. Instead, our observations suggest that the nozzle holes should be considered partially filled with a dense fluid.

1. Introduction

The importance of the problem of spray breakup for various applications is well recognised and has been extensively studied experimentally and theoretically [1–9]. A rigorous theory of spray breakup would be very complex as it would need to involve modelling of nozzle flow, cavitation, instabilities, the initial formation of ligaments and droplets and their subsequent breakup, evaporation, the entrainment of air and the effects of turbulence [3]. Experimental characterisation of the initial stage of diesel jet formation and primary breakup under realistic engine conditions is challenging due to the harsh environment in which they take place. This inherent complexity is compounded by the highly transient nature of the processes involved, along with the elevated velocities and the microscopic scale at which they occur. Direct visualisation techniques are invaluable to improve the fundamental understanding of primary breakup but because of the challenges posed by the conditions under which diesel jets occur, simplified experiments are often used to infer breakup characteristics at normal operating conditions. In particular, the injection and gas pressures are often reduced, the injector geometry simplified, and the fuel replaced by a more convenient fluid.

* Corresponding author. Tel.: +44 1273 642 312.
E-mail address: c.crua@brighton.ac.uk (C. Crua).
URL: http://www.brighton.ac.uk/cae/crua (C. Crua).

http://dx.doi.org/10.1016/j.fuel.2015.04.041
0016-2361/

Microscopic imaging experiments of diesel sprays have been reported in the literature (e.g. [5,10–13]), although at atmospheric conditions and with varying degrees in the quality of the images produced. Satisfactory lighting can be particularly difficult to obtain at microscopic level. High-power short duration laser pulses may seem appropriate, but speckle patterns caused by the interference of reflections of such coherent monochromatic light conceal the underlying morphology of the spray, thus significantly degrading the quality of the resulting images and making their interpretation limited. Such optical artifacts can be observed in images recorded by Lai et al. [11], Badock et al. [12] and Heimgärtner & Leipertz [5], for example. Speckle patterns can be avoided by using a spark light instead of a laser, but the duration of the spark flashes are significantly longer and lead to motion blurring, even at low spray velocities, unless the exposure can be accurately controlled by the imaging device. The relatively long and random jitter associated with the timing of the spark can also lead to a significant proportion of 'missed' acquisitions which, combined with the long recharge time of the high-voltage electronics, may significantly lengthen the experimental work. The LED technology has advanced rapidly, and can now provide low-jitter sub-nanosecond [14] and high-frequency light pulses [15]. However, the energy output of high-power LEDs is still insufficient to enable blur-free microscopic imaging of high-speed sprays. The challenging lighting requirements for such experiments has limited their application to atmospheric conditions, with the exception of our preliminary studies [16–19], and the recent work of Manin et al. [20]. Additional complications introduced in high pressure and temperature environments include the presence of turbulence, density and temperature gradients in the gas phase, which will result in refractive index fluctuations.

In this study we present high-resolution microscopic, as well as ultra-high-speed, images of diesel sprays at both atmospheric and diesel engine-like operating conditions. The still images were obtained by spectrally diffusing a Nd:YAG laser pulse and provide high-resolution blur-free observations of the injection process at a microscopic scale. A limitation associated with still imaging is the inherent lack of information on the spatio-temporal evolution of the transient jet and droplets observed. Specifically, there is no information on the velocity field, a quantity which is of particular significance for the investigation of breakup and essential for the approximation of relevant parameters such as the Weber and Reynolds numbers. In order to complement the fine spatial information derived from the still images, an ultra-fast framing camera was then used to accurately record the temporal evolution of diesel sprays at microscopic scales, with a second high speed camera simultaneously recording the macroscopic evolution of the complete spray. This allowed a precise tracking of the temporal evolution of diesel jets from the actual start of fuel delivery, thus eliminating the timing uncertainty associated with single images. This is particularly relevant when the transient jets being observed evolve over a shorter timescale than the mechanical and hydraulic jitters associated with solenoid-actuated servo-valve diesel injectors.

2. Experimental configurations and data acquisition

2.1. Rapid compression machine

The experiments were carried out using a reciprocating rapid compression machine (RCM) based around a Ricardo Proteus single cylinder engine converted to liner-ported, 2-stroke cycle operation [21]. The removal of the valve train allowed the fitting of an optical chamber of 80 mm in height and 50 mm diameter into the cylinder head. The optical access to the combustion chamber was provided by three removable sapphire glass windows. Due to the increased volume of the combustion chamber the compression ratio was reduced to 9:1. To simulate a real diesel engine with a compression ratio of 19:1, the intake air was conditioned to give in-cylinder pressures and temperatures up to 8 MPa and 540 K, respectively. For the present experiments the peak in-cylinder temperature was intentionally kept low in order to inhibit autoignition. Prior to motoring the RCM, the cylinder head was heated by a water jacket to 85 °C and immersion heaters heated the oil to 40 °C. The RCM was motored by a dynamometer to 500 rpm, and kept at stable in-cylinder conditions for the duration of the recordings. Scavenging on the in-cylinder gases was done by skipping injections for several cycles. This approach still allowed an acquisition frequency of several fuel injections per second. The test conditions are summarised in Table 1, including the in-cylinder motored peak pressure, gas temperature and injection pressure. For each condition, microscopic images were recorded at a range of locations within the spray.

2.2. Fuel injection equipment

The fuel was delivered by a Delphi common-rail system, comprising a DFP-3 high-pressure pump rated at 200 MPa, and a seven hole DFI-1.3 injector with a VCO type nozzle. The high-pressure rail and the delivery pipe were both instrumented with pressure transducers. The rail pressure, timing and duration of the injection were independently controlled by a purpose-built EmTronix fuel injection controller. The nozzle's orifices were cylindrical with a diameter of 135 μm and a length of 1 mm. The nozzle had an equivalent cone angle of 154°, and the injector was mounted horizontally relative to the cameras. This injector was extensively characterised on a macroscopic scale by high-speed video and laser diagnostics [22]. Since the focus of this study is on the initial spray formation, and as all images were captured long before the end of the injection event, it was not necessary to control the total mass of injected fuel. Instead, an injector trigger pulse with a fixed duration of 550 μs was used for all conditions.

The fuels, listed in Table 2, were chosen to obtain a wide range of physical properties. The fossil diesel fuel was an ultra-low sulphur, non-additised, reference fuel representative of automotive diesel. The RME, compared to the fossil diesel, has a substantially increased viscosity and lubricity with a small increase in surface tension. Kerosene was chosen for its opposite trend in physical properties compared to RME, which can assist to indirectly substantiate comparisons between RME and fossil diesel.

2.3. High-resolution microscopy

The optical experimental setup is shown in Fig. 1. The pump light source used for still imaging conditions was a frequency-doubled Nd:YAG laser with a pulse duration of 7 ns. The light pulse was spectrally broadened using a fluorescence diffuser, and spatially expanded from 8 mm to 100 mm in order to provide homogeneous illumination over a sufficiently large area, with an effective exposure of 20 ns. Two dual-frame Peltier-cooled 12 bit CCD cameras were used to simultaneously visualise the sprays at the microscopic and macroscopic scales. The camera facing the light source was fitted

Table 1
Operating conditions for microscopic imaging.

Gas pressure (MPa)	Gas temperature (K)	Injection pressures (MPa)
0.1 MPa	293	40; 100
4 MPa	540	40; 100; 160
6 MPa	540	40; 100; 160
8 MPa	540	40; 100; 160

Table 2
Physical properties of fuels tested.

Physical property	RME	Diesel	Kerosene
Viscosity ($mm^2\ s^{-1}$)	4.4	3.3	1.2
Density ($kg\ m^{-3}$)	883	837	803
Surface tension ($mN\ m^{-1}$)	33.2	30	27.7
Lubricity (μm WSD)	180	500	710
Sulphur content ($mg\ kg^{-1}$)	–	<0.5	<0.5
PAH content (% m/m)	-	4.2	2.1
FAME content (% v/v)	100	<0.5	<0.5

with a long range microscope with a 12 cm working distance, and optics were selected to obtain a magnification factor of 10.8 at the CCD sensor plane. Hence the scale factor was 0.6 μm per pixel, and the viewing region was 768 × 614 μm. The second CCD camera was located orthogonally to the light source and provided a simultaneous macroscopic view of the 7 sprays. Images were recorded for 44 different spatial locations covering the initial stages of spray formation, the evolution of the spray boundary at the tip and at the periphery of the jet, as well as some optically-thin internal regions where the transition from liquid jet to atomised spray occurs.

2.4. Ultra-high-speed microscopy

In order to record the velocity of the sprays and to observe their transient behaviour, the CCD cameras were replaced by two high-speed video cameras. The ultra-fast framing camera was a Specialised Imaging SIM-16 camera, capable of recording 16 intensified images with no inter-frame delay. The SIM-16 has an equivalent acquisition rate of up to 200 million frames per second, at a fixed resolution of 1280 × 960 pixels with 12 bit dynamic range. Each frame featured an independent acquisition delay, exposure duration and intensifier gain. The ultra-fast framing camera was fitted with the long range microscope, resulting in an effective viewing region of 995 × 746 μm. It faced the light source, hence producing shadowgraphic images of the diesel sprays. The exposure time was adjusted as necessary between 20 ns and 200 ns in order to minimise motion blurring. Some blurring still occasionally occurred as a result of out-of-plane droplets and a particularly shallow depth of field (approx. 20 μm).

A second high-speed camera was located orthogonally to the light source and recorded the full evolution of the spray on a macroscopic scale simultaneously to the ultra-fast framing camera. Its acquisition speed was set to 94500 images per second, with a resolution of 24 × 192 pixels and a viewing region of 5 × 35 mm. This second camera was used to measure the evolution of spray penetration with time.

For the video recordings, the illumination of the sprays was achieved by a 500 joule xenon flashgun (Specialised Imaging AD500) which delivered a 2 ms light pulse. This duration was sufficiently long to allow the recording of the complete injection event by the macroscopic camera, and bright enough to achieve exposures of 20 ns with the microscopic camera.

3. Results and discussion

In this section we first present measurements obtained at atmospheric conditions, followed by measurements obtained at elevated pressure and temperature conditions. The formation and breakup of diesel jets are commonly studied at atmospheric conditions, especially as a first step towards the development of a new optical diagnostic [23], or when a particular measurement technique cannot be applied reliably at engine conditions. In any case, results of studies on diesel breakup at atmospheric conditions cannot be expected to be fully representative of atomisation under normal engine operating conditions. However, we will show in this section that our measurements at standard pressure and temperature can give some valuable insights into the physical processes involved in the initial jet formation at realistic engine conditions.

3.1. Emergence of fuel from the orifice

Fig. 2 shows the evolution of the fossil diesel sprays at atmospheric conditions, with injection pressures of 40 and 100 MPa. Although an injection pressure of 40 MPa is relatively low in the operating range of modern diesel common-rail systems, it represents an important test point for light load and idle stability. The

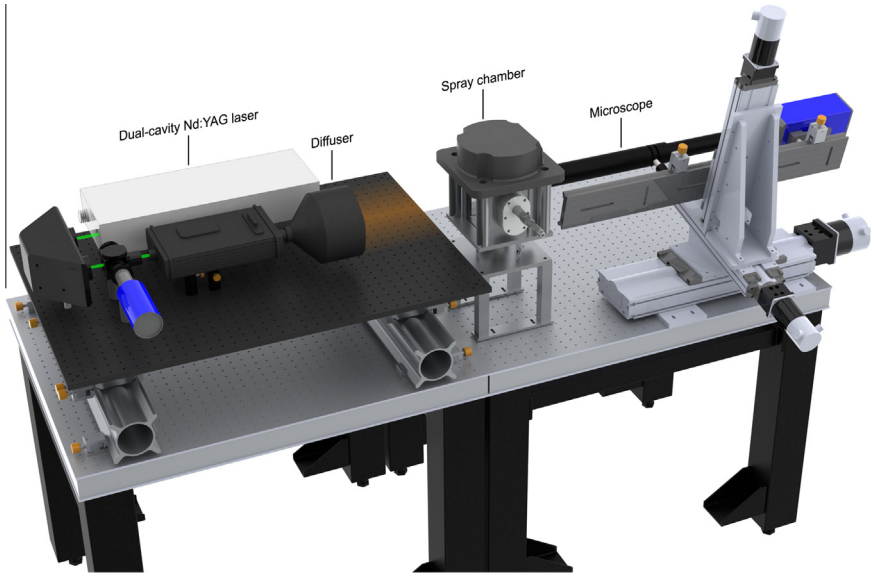

Fig. 1. Optical setup for high-resolution microscopic imaging on the atmospheric spray chamber. The CCD camera and microscope were mounted on a 3-axis electronic traverse with 3 μm positioning accuracy. A dual-cavity Nd:YAG laser pumped a fluorescing diffuser to provide a speckle-free 20 ns light pulse. A second CCD camera (not shown) faced the injector nozzle and provided a simultaneous macroscopic view of the 7 sprays. For the high pressure conditions, the optical setup was transferred onto the reciprocating rapid compression machine described in Ref. [21].

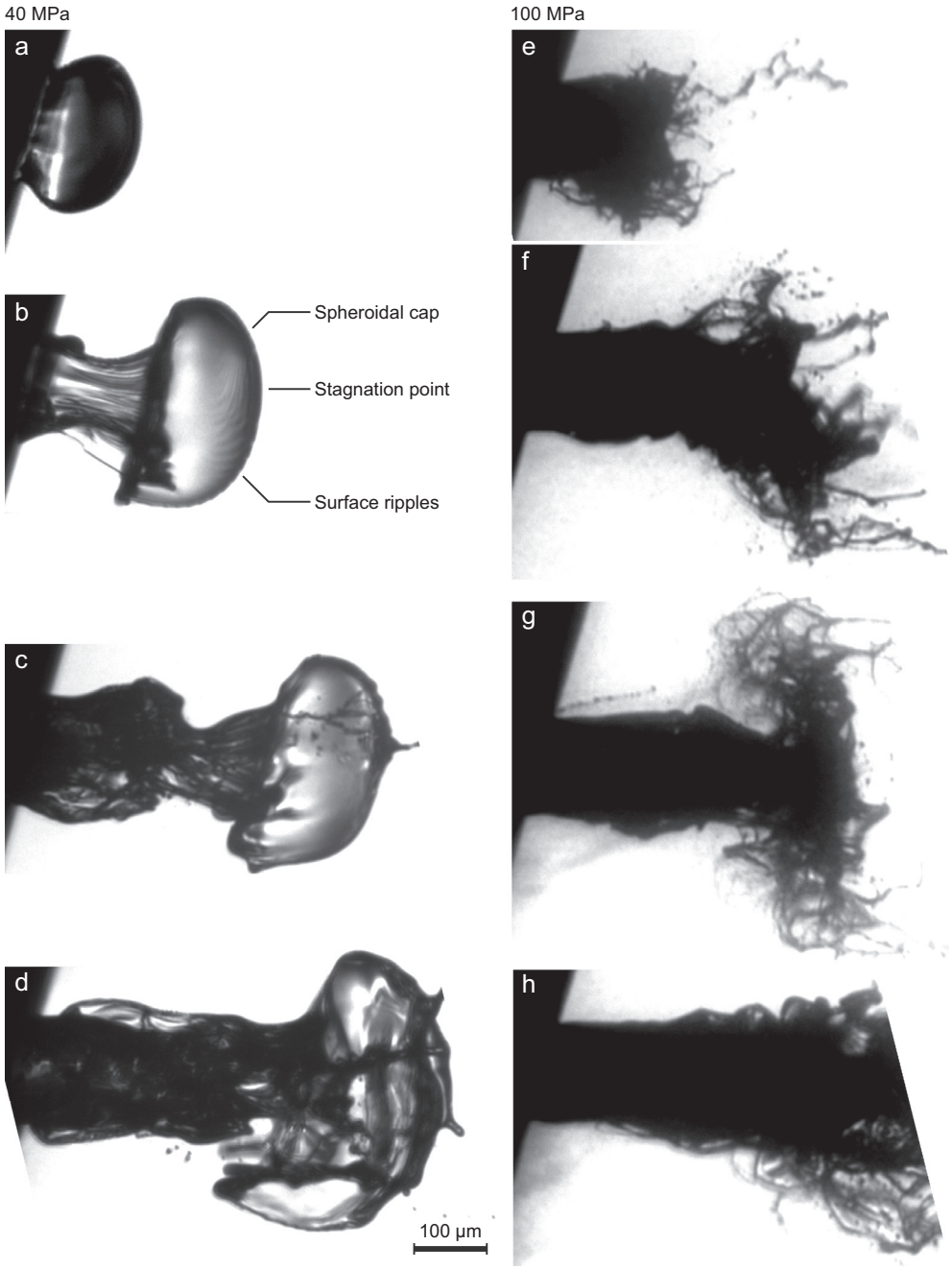

Fig. 2. Effect of injection pressure on the initial stage of diesel fuel injection at atmospheric pressure and temperature conditions.

images were rotated so that the nozzle orifice being observed in Fig. 2 lies horizontally. The jets observed in Fig. 2 evolved over a shorter timescale than the mechanical and hydraulic jitters associated with this particular injector model, hence timings for individual images could not be resolved. In Fig. 2a and b the emerging liquid fuel takes the shape of an undisrupted oblate spheroid. The radial expansion of the jet is quite noticeable and explanations for this behaviour which were considered, but discarded, included the presence of cavitation bubbles within the jet, the aerodynamic interaction with the surrounding gas, and the slight compressibility of diesel fuel.

The effect of gravity on the shape of the jet is intuitively ruled out, and this can easily be confirmed by calculating the capillary length, defined as $\sqrt{\sigma/\rho g_0}$. At the temperatures and pressures used in this investigation, the capillary length for diesel fuel is between 1 and 1.9 mm. Since the characteristic lengths for this experiment are well below this value, it is confirmed that gravity has no influence on the shape of the initial fuel jet. The possible presence of cavitation bubbles within the jet was rebutted by the fact that cavitation is unlikely to be established at such an early stage of the injection process, and that no signs of gaseous bubbles were detected in the subsequent images and videos. For example in Fig. 2b the head of the mushroom-like jet, as observed and described by Badock et al. [12], is evidently free of gas as internal impurities would be clearly observed there. The aerodynamic interaction with the gas, potentially inducing a deceleration of the tip of the liquid fuel and a radial expansion can be ruled out due to the low density of the surrounding gas at ambient conditions, giving a liquid–gas density ratio of 695. The compressibility of diesel fuel is rather small and can be neglected as the volumetric

expansion associated with a 40 MPa pressure drop at the nozzle exit is less than 2%. The radial expansion of the jet in Fig. 2a can be explained by the initial acceleration of the injected fuel during the needle lift, and the laminar flow condition observed at the nozzle exit. In that respect, the radial expansion is an indication of the spheroidal drop being inflated by the upstream fuel, and stabilised by surface tension.

Ultra-high-speed videos indicated that for these conditions the fuel emerged from the nozzle orifice with a velocity of 16 m s^{-1}. This relatively low initial velocity implies that the inertial forces at the nozzle exit may be small compared to the surface tension forces, at least at the early stage of injection. The balance of inertial and surface tension forces is defined by the Weber number, which can be calculated in the present case using the gas and liquid densities:

$$We_g = \frac{\rho_g v^2 d}{\sigma} \quad \text{and} \quad We_\ell = \frac{\rho_\ell v^2 d}{\sigma} \tag{1}$$

with ρ_g the density of the gas (1.2 kg m^{-3}), ρ_ℓ the density of the fuel, v the exit velocity of the fuel (16 m s^{-1}), d the orifice diameter (135 μm) and σ the surface tension of the fuel, giving $We_g = 1.4$ and $We_\ell = 964$. Using the kinematic viscosity from Table 2 the Reynolds number can be calculated for these conditions as 663. These values support the assumption that the jet in Fig. 2a is laminar and the observation that it is not inclined to breakup. In contrast, the 100 MPa jets in Fig. 2e–h appear to be turbulent and partially atomised. This agrees with a measured average tip velocity of approximately 100 m s^{-1}, and the correspondingly higher We_g (≈54), We_ℓ (≈37 700) and Re (≈4 100) which indicate that the flow is both in the atomisation regime and turbulent.

In effect, the radial expansion of the liquid jet was often sufficient in magnitude for the oblate spheroid to stick to the nozzle surface with a large contact angle, similarly to a sessile drop resting on a hydrophobic surface. It should be noted that the inertial forces are small but not negligible, and can be assumed to be responsible for the apparent large contact angle between the liquid fuel and the nozzle surface. As the injection velocity increases rapidly, the inertial forces become sufficient to detach the droplet from the nozzle surface. This can be seen in Fig. 2b where the tip of the fuel jet takes the shape of a spheroidal cap, with its base still parallel to the nozzle surface. The striations of the jet leading to the spherical cap are likely to be a sign of the stretching caused by the sudden detachment of the cap from the nozzle. Tests conducted on the RCM at in-cylinder pressures (ICP) of 0.1, 4, 6 and 8 MPa showed that these structures are much more recurrent as the ICP was increased, indicating that the increased density of the surrounding gas slows down the penetration of the jet, thus further promoting an initial radial expansion. Similar images were obtained by Badock et al. [12] with a single-hole injector, for an injection pressure of 25 MPa and gas pressure of 1.5 MPa, and described as stochastic mushroom-like structures. It is now evident that the spheroidal caps observed by Badock et al. and in Fig. 2 are formed by the combination of radial jet expansion and are function of the physical properties of the fuel. It is now also evident that their occurrence is not limited to customised injectors and fluids, and that they occur in production injectors and with real diesel fuels.

A stagnation point can be seen on the tip of this spheroidal cap (Fig. 2b), where the liquid boundary meets the horizontal axis of symmetry of the nozzle orifice. Ripples can be observed surrounding the stagnation point on the interface of the cap, which are possibly caused by shearing instabilities at the boundary between the liquid and gas interface. The wavelength associated with these surface ripples ranged between 3 and 8 μm and are proposed to be the result of a short-lived Kelvin–Helmholtz type instability. The occurrence of these interfacial disturbances indicates that a shear layer on the liquid side of the interface is also likely to exist. The ripples are particularly noticeable on the lower liquid boundary in Fig. 2b, and appear to be oriented perpendicularly to the shear. This, in turn, would suggest the presence of a toroidal internal motion within the spheroidal cap. The outer surface of the cap rapidly becomes unstable and starts disintegrating (Fig. 2d), eventually leading to the formation of ligaments which break up into droplets through hydrodynamic and capillary instabilities. The disintegration of the cap does not result from the aforementioned Kelvin–Helmholtz ripples, but from the presence of a faster internal jet within the spheroidal cap. The evidence leading to this conclusion will be discussed next.

By recording the evolution of the fuel jets with an ultra-high-speed camera, the evolution of the residual and fresh fuel could be observed through time for single injection events. Fig. 3 shows a video sequence recorded at 1280 × 960 pixels, with 20 ns exposures and a fixed interframe delay of 2 μs. On these videos the residual fuel has a translucent appearance which can be explained by the relatively undisturbed interface between the liquid fuel and surrounding air, which facilitates the refraction of light towards the camera. The fresh fuel takes a darker appearance, and can be seen emerging from the nozzle at frame 5 in Fig. 3. This discontinuity in the refraction of the light allowed the residual and fresh fuel to be independently tracked.

Fig. 4 shows a series of images selected from an ultra-high-speed video sequence recorded at evaporating conditions. It should be remarked that although the *pixel* resolution of the ultra-fast framing camera is relatively high (1280 × 960 pixels) the *spatial* resolution is degraded as a result of the image intensification process. This explains why the fine details of the spray are not resolved as well as with the high-resolution microscopy images. The spatial resolution of the ultra-fast framing camera could have been improved with a brighter light source, which would have allowed the use of lower gain values for the camera's image intensifiers. Fig. 4 illustrates the interaction between the spheroidal cap and the liquid jet that follows. Although still apparent, the spheroidal cap is much less distinguishable than at non-evaporating conditions, as can be seen on Fig. 4a. Further investigations led to the conclusion that at elevated in-cylinder temperatures the spheroidal cap is in vapour state, and can be observed due to the refraction of the light caused by density gradients. Indeed, the light intensity in shadowgraphy is linked to the second spatial derivative of the refractive index [24]. This effect offers the benefit of allowing the distinction to be made between the spheroidal cap and the inner jet that disintegrates it, a distinction which cannot be made under non evaporating conditions such as in Fig. 2. The jet that forces the cap to detach from the nozzle surface in Fig. 4b–d is opaque indicating that it is in liquid state, while the spheroidal cap is already vapourised.

A thin ligament is formed in Fig. 4c on the tip of the liquid jet, within the vapour cap. This central ligament stretches ahead of the main jet and can be seen to perforate the cap in Fig. 4d. The formation of this thin ligament indicates that the velocity ahead of the tip of the jet, on the axis of symmetry, is significantly higher than on the periphery of the jet. This leads us to the conclusion that the internal motion of the nozzle-trapped vapour must be toroidal prior to its disintegration. This corroborates the hypothesis we made based on the observation of ripples on the surface of the liquid in Fig. 2b. The vortex ring motion within the vapourised fuel resulted in a slipstream effect which led to a thin central ligament being propelled ahead of the liquid jet.

Fig. 5 shows the same process recorded by high-resolution still imaging, with a central ligament visibly propelled ahead of the jet as a result of the vortex ring motion in the spheroidal cap. The diameter of the ligament was measured to be 23 μm in this

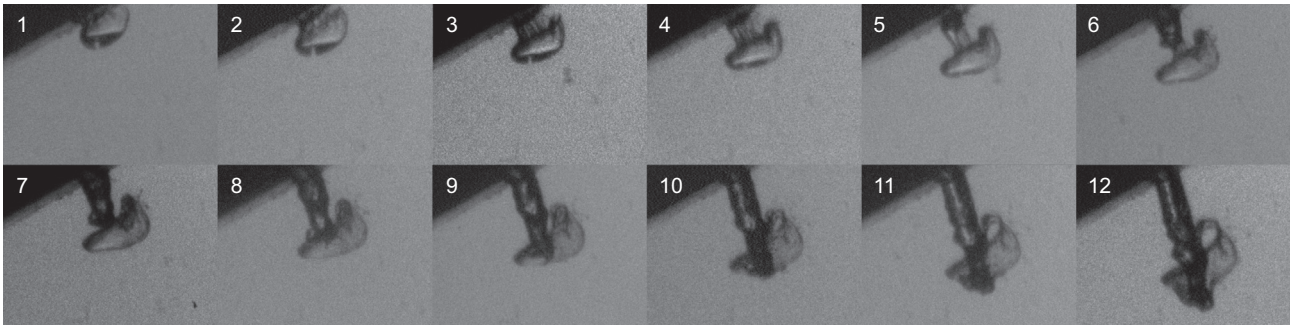

Fig. 3. Ultra-high-speed video sequence of diesel fuel injected at 40 MPa into atmospheric pressure and temperature conditions, recorded at 500 kHz with 20 ns exposures. The translucent appearance of the residual fuel (frames 1–4) allowed the fresh fuel to be independently tracked as it penetrates through the residual liquid fuel (frames 5–12). See [29] or supplemental material for the full video [29].

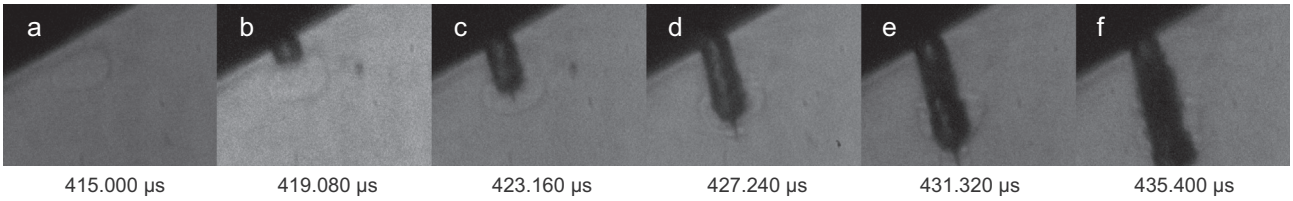

Fig. 4. Interaction between nozzle-trapped vapour and a liquid diesel jet, leading to the propulsion of a ligament ahead of the main liquid jet. The propulsion of the liquid jet indicates the presence of a vortex ring structure inside the vapour. Injection pressure is 40 MPa; gas pressure is 4 MPa. Timings are relative to start of injection trigger pulse. See [29] or supplemental material for the full video.

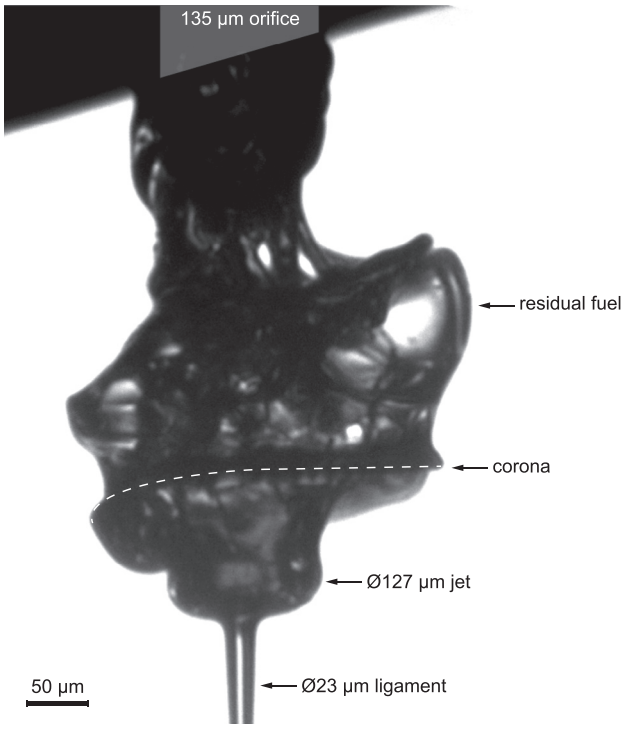

Fig. 5. A 23 µm ligament is propelled ahead of the jet by the vortex ring motion inside the residual fuel. The jet seen in Fig. 4d at the base of the ligament is also visible here with a diameter of 127 µm, marginally smaller that the orifice diameter (135 µm) overlaid at the top of the image. A corona is formed as a result of the residual fluid being punctured by the high-speed jet. Injection pressure is 40 MPa; gas pressure is 0.1 MPa.

instance. It can also be observed that the jet seen in Fig. 4d at the base of the ligament is also visible in Fig. 5 with a diameter of 127 µm. The jet appears to have just perforated the tip of the spheroidal cap, and thereby created a short corona whose rim can be seen on the surface of the spheroidal cap. Similar coronas can be seen in Fig. 2d and, albeit less noticeably, in Fig. 4d.

Consequently, we propose that the spheroidal cap consists of residual fluid, trapped inside the nozzle orifices and expulsed at the beginning of injection. At atmospheric conditions this residual fluid consists of liquid fuel. At engine conditions the residual fluid is gaseous, most likely consisting of a mixture of vapourised fuel and ambient gas. To test the possibility of this process we estimated the volume of the cap from our images, by assuming axial symmetry, and found it represented between 50% and 83% of the orifice's volume. This confirms that the volume of fluid that makes up the spheroidal cap can exist as trapped fluid inside an orifice of the nozzle. Hence we propose that the similar, but previously unexplained, observations made by Badock et al. [12] and Roisman et al. [25] of central ligaments present downstream of diesel sprays are a result of vortex ring motion created by the expulsion of nozzle-trapped fluid. Additionally, we have shown that this phenomenon is not specific to single-hole nozzles, but also occurs in the latest generation of production injectors.

We could not measure the hydrocarbon content of the trapped vapourised fluid, but careful observation of the shadowgraphs can yield information on the fluid's density relative to that of the surrounding gas. First, we consider that whilst the intensities in a Schlieren image are indicative of the *first* spatial derivative of the refractive index field, a correctly formed shadowgraph has intensities related to the *second* spatial derivative of the refractive index (i.e. $\partial^2 n/\partial x^2$) [24]. Since the refractive index of a gas is function of its density, the intensities in a shadowgraph are related to the second spatial derivative of density. This effect can be observed in Fig. 6, where a step change in gas density along the interface always results in a pair of bright and dark fringes. When plotting the intensities along the profile AA in Fig. 6, the bright fringes appear at the ambient gas' side, whilst the dark fringes appear on the residual fluid's side. This indicates that $\partial^2 n/\partial x^2$ increases from the ambient gas to the residual fluid, which in turn shows that the density also increases along that direction. We conclude from this

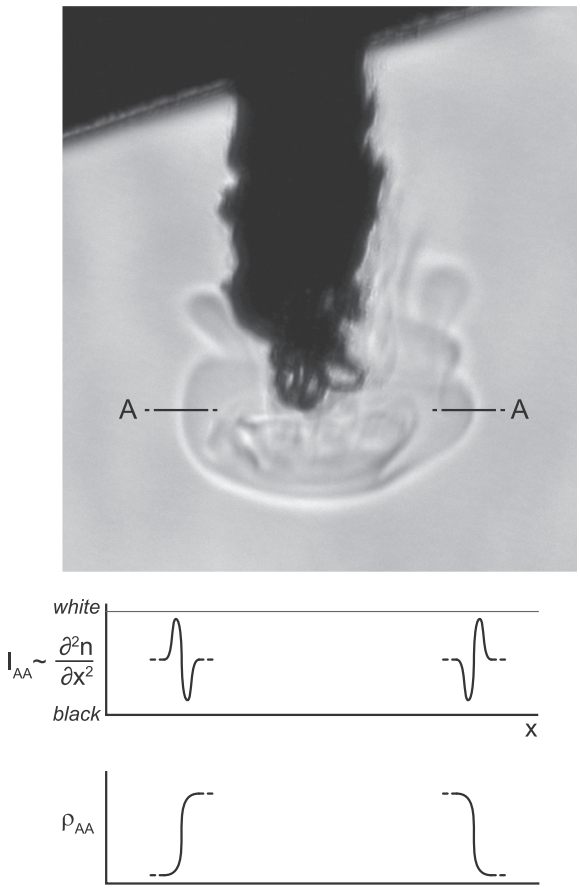

Fig. 6. High-resolution microscopic image of diesel fuel injected at 40 MPa into 3.2 MPa. The intensities of a shadowgraph are related to the second spatial derivative of the refractive index field. Plotting the intensities I_{AA} along the profile AA shows that the bright fringes appear on the ambient gas' side, whilst the dark fringes appear on the residual fluid's side. This indicates that $\partial^2 n/\partial x^2$ increases from the ambient gas to the residual fluid, which in turn shows that density also increases along that direction. Hence the residual fluid must be denser than the surrounding gas.

analysis that the residual fluid must be denser than the surrounding in-cylinder gas.

3.2. Effect of fuel properties

In Fig. 7 we now demonstrate the effect of fuel properties on the initial jet formation by showing three fuels injected at 40 MPa into atmospheric conditions. As discussed previously, the fossil diesel exits the nozzle as an undisturbed oblate spheroid which was identified as trapped fuel left over from the previous injection. Fresh fuel from the new injection forces the trapped fluid out, causing it to eventually lift off the surface of the nozzle. The residual fluid travels further into the chamber, before being disintegrated by the fresh fuel. Compared to the fossil diesel, the RME jet appears to resist deformation, most likely due to the increased surface tension (11%) and viscosity (36%), which are expected to exert a stabilising force on the liquid jet. As can be seen in Fig. 7, the residual RME fuel appears to maintain its spheroidal shape for a longer distance, and disintegrates at a later time compared to the fossil diesel.

The residual kerosene fuel exits the nozzle with a more opaque appearance in Fig. 7a, indicating that the interface between the gas and liquid is more complex and unstable. Ligaments and droplets can be seen to form almost the instant the jet exits the nozzle (Fig. 7b). When the fresh fuel penetrates through the residual fuel, the disturbances caused result in an inability of the residual fuel to maintain the shape of a spheroid. In Fig. 7c the presence of ligaments can be seen on the periphery of the fresh kerosene jet, which were not identified for the fossil diesel or RME. These observations of primary atomisation clearly illustrate the stabilising force of viscosity and surface tension on the initial formation of high-pressure fuel jets, and the impact on the formation of ligaments, droplets and instabilities.

These observations tie in when comparing the estimates for the liquid jets' Weber and Reynolds numbers. The balance of inertial and surface tension forces is defined by the Weber number, which can be calculated using either the gas or liquid density. The characteristic length used was that of the nozzle orifice diameter (135 μm). As the air inside the rapid compression machine is quiescent [21] the gas velocity is negligible.

For fossil diesel ($\rho_\ell = 837\ \mathrm{kg\ m^{-3}}$; $\rho_g = 1.2\ \mathrm{kg\ m^{-3}}$, the exit velocity of the jet piercing the residual fluid $v = 43.7\ \mathrm{m\ s^{-1}}$, and $\sigma = 29.8\ \mathrm{mN\ m^{-1}}$), we find that We_g is equal to 10 and We_ℓ is 7 049. These Weber numbers give a relative comparison of the fuel jets' propensity to atomise, and indicate that the fossil diesel jet is in a first-wind induced breakup regime [1]. The Reynolds number ($Re = vd/\nu$), a measure of the ratio of inertial forces to viscous forces, can be estimated at 1 810. This indicates that the fuel jet is laminar but close to the transitional region. The relatively undisturbed appearance of the RME jet is explained by calculating its Reynolds number. Near the orifice at the start of injection the leading edge velocity was measured at $28.3\ \mathrm{m\ s^{-1}}$. At these conditions $Re = 868, We_g = 3.4$ and $We_\ell = 2\ 471$. This explains the laminar flow observed at the early stages of injection.

The data from the ultra-high-speed images of the kerosene jets corroborate with the values estimated for the fossil diesel and RME. The Re of 4 878, We_g of 11 and a We_ℓ of 7 236 were estimated using the initial velocity of the fresh fuel ($43\ \mathrm{m\ s^{-1}}$). This confirms that the flow is turbulent with a propensity to disintegrate.

Fig. 8 shows the evolution of jet tip penetration with time, for kerosene, fossil diesel and RME, derived from these videos. For the RME jet the distinction between residual and fresh fuel could not be made, and the tip of the fresh fuel was not plotted. Fig. 8 indicates that the kerosene emerges earlier than the other fuels, which can be attributed to lower frictional losses between the fuel and the nozzle surface. RME emerged later than the other fuels. In spite of its relatively high lubricity, which should reduce friction in the nozzle, the viscosity and surface tension of RME appear to play a more dominant role on frictional losses in the nozzle [26].

Fig. 9 shows the effect of fuel properties on the sprays' structures as they undergo primary atomisation. The effect of aerodynamic forces on atomisation have a negligible influence on the breakup of cylindrical jets at low ambient pressures, when the ratio of the liquid and gas density is above 500. Thus for atmospheric ambient pressures, in the region before the onset of breakup, the turbulence of the jet and fuel properties are the key factors that influence initial stages of breakup. In the case of RME, the viscous forces resist the formation of ligaments and droplets, resulting in a stabilising effect on the jet. The simultaneous increase in viscosity, surface tension and lubricity leads to a notable decreased rate of atomisation.

Between 1 and 1.6 mm downstream from the nozzle, soon after the leading edge passes, the lack of ligaments and droplets around the RME jet is clearly evident compared to the fossil diesel and kerosene. The ligaments that are produced from RME are markedly larger than for the other fuels.

3.3. The dynamics of the initial jet formation

Figs. 10 and 11 show the effect of injection pressure on the evolution of liquid spray penetration with time, obtained from the

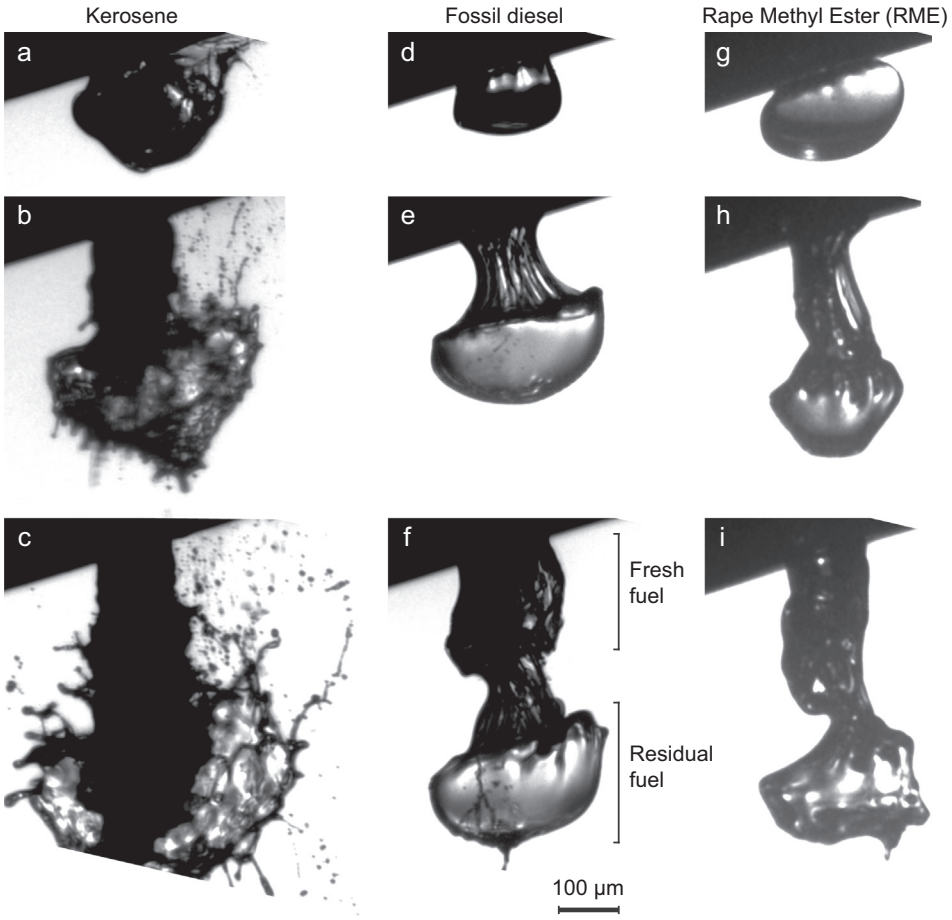

Fig. 7. Influence of fuel type on the initial jet formation of kerosene, fossil diesel and RME fuels injected at 40 MPa into atmospheric pressure and temperature conditions. The kerosene jets exhibit primary atomisation within 200 µm of the nozzle exit. The fossil diesel, and to a larger extent the RME jets, resist deformation due to their higher surface tension and viscosity.

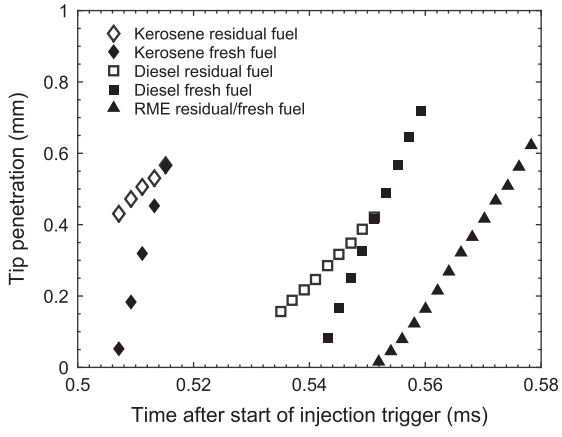

Fig. 8. Penetrations of kerosene, fossil diesel and RME fuels injected at 40 MPa into atmospheric pressure and temperature conditions. The plots for the diesel fuel were obtained from the video presented in Fig. 3.

simultaneous video recording of single spray events at macroscopic and microscopic scales. Tip penetration measurements were obtained from every frame of the microscopic ultra-fast framing videos, both for the residual fluid and the subsequent jet. In Figs. 10 and 11 the solid lines represent the penetration of the trapped fluid, while the dotted lines represent the penetration of the jet. Once the jet has overtaken the residual fluid, as in Fig. 4d for example, only the jet's penetration is plotted as the residual fluid disintegrates and can no longer be tracked as a single volume of fluid.

The macroscopic evolutions follow the well documented two stage spray penetration profile [27,28]. The first stage is a linear evolution of spray penetration with time, which can be observed on Fig. 11a between 0.38 and 0.45 ms for 160 MPa injection pressure. During the second stage, from 0.45 ms onward in Fig. 11a for 160 MPa, the spray tip velocity reduces and the penetration follows a square-root temporal dependence.

Whereas the macroscopic measurements are in agreement with the literature, it is interesting to note that the microscopic scale observations indicate that the initial stage of fuel injection is more complex than the previously reported linear evolution. Indeed, while the microscopic jet follows the expected linear macroscopic evolution, to the best of our knowledge the precursory residual fluid does not follow previously reported temporal trends. The trapped fluid's tip propagates at a noticeably slower rate than the subsequent liquid jet, and represents a preliminary, albeit much shorter, phase to the accepted two stage diesel spray penetration profile. Most previous experiments failed to observe the residual fluid's propagation due to unrealistic operating conditions and the lack of sufficiently high spatial and temporal resolutions. While the liquid jet is opaque and observable by light scattering techniques, the residual fluid that precedes it is in vapour state and only visible when using optical diagnostics which are sensitive to density gradients, such as shadowgraphy and Schlieren imaging.

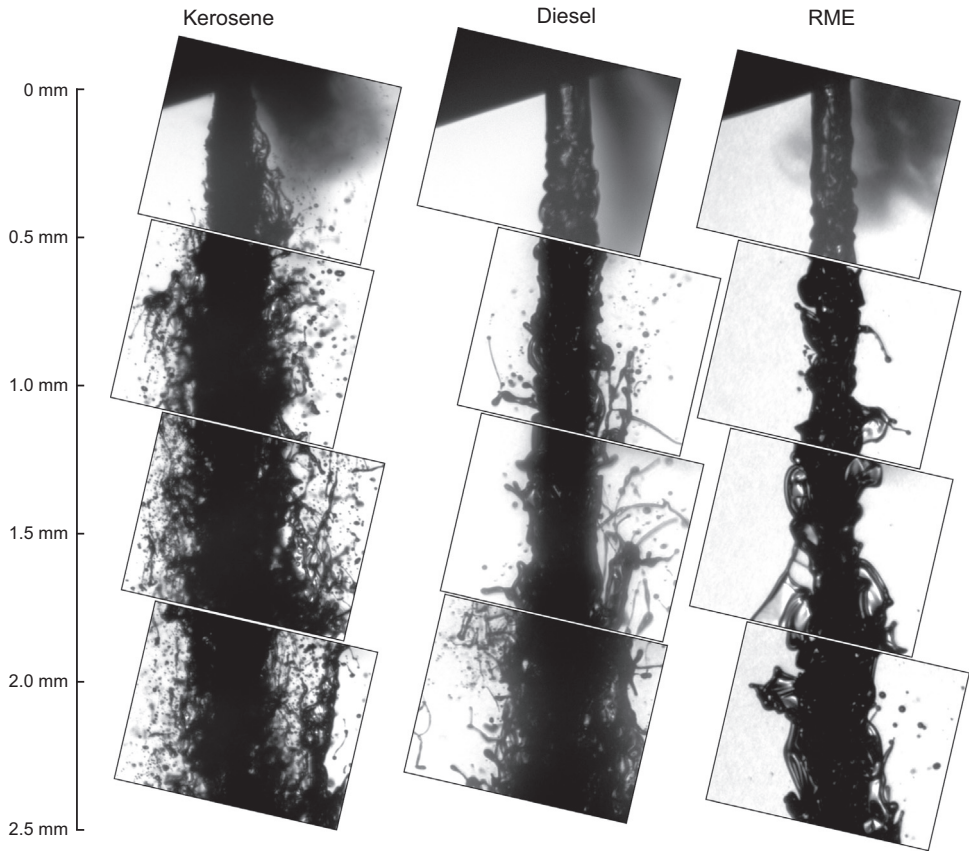

Fig. 9. Influence of fuel type on the primary atomisation within the first 2.1 mm from the nozzle. Each row represents the same spatial location. Injection pressure is 40 MPa; gas pressure is 0.1 MPa.

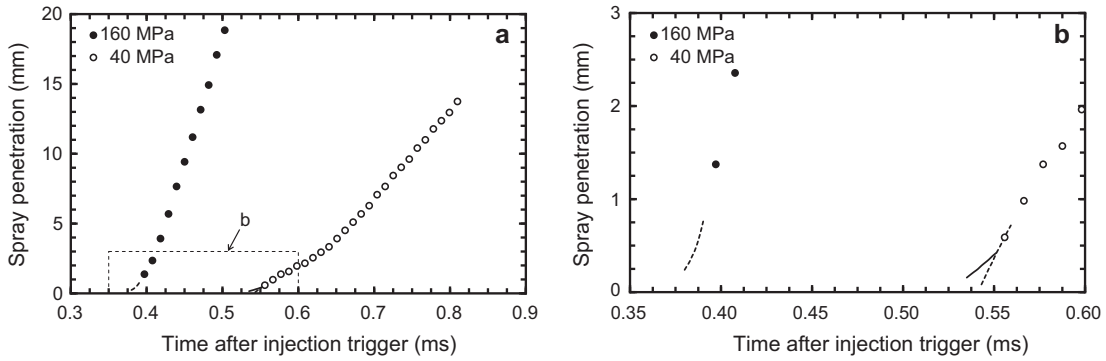

Fig. 10. Evolution of liquid spray penetration with time for diesel fuel injected into atmospheric condition at two injection pressures, recorded at macroscopic (a) and microscopic (b) scales simultaneously. Solid lines represent the trapped fluid's penetration, and the dotted lines the liquid jet's.

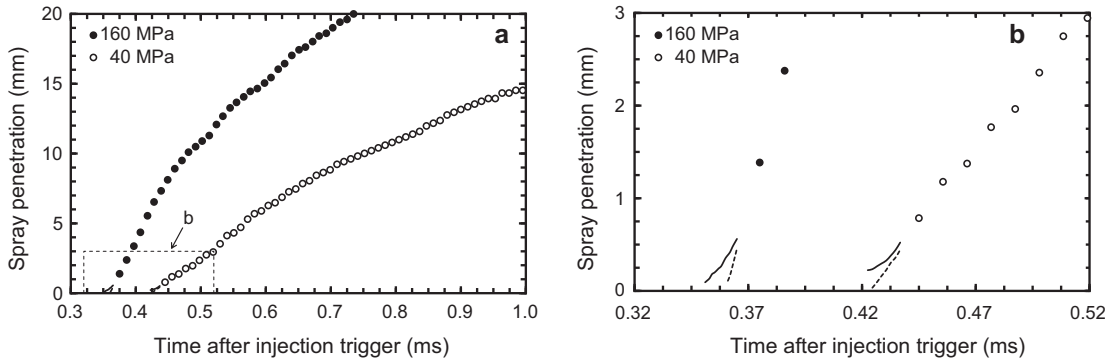

Fig. 11. Evolution of liquid spray penetration with time for diesel fuel injected into 4 MPa gas pressure, recorded at macroscopic (a) and microscopic (b) scales simultaneously. Solid lines represent the trapped fluid's penetration, and the dotted lines the liquid jet's.

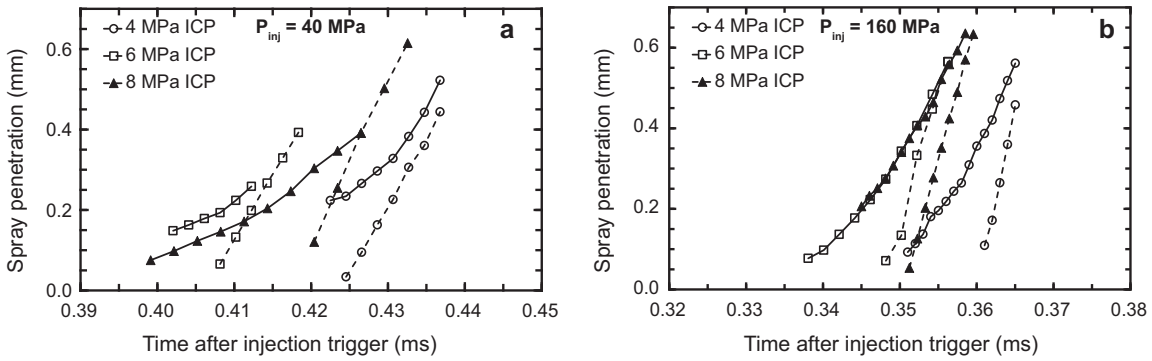

Fig. 12. Initial spray penetrations obtained from ultra-high-speed videos recorded at 500 000 frames per second. The diesel fuel was injected at 40 MPa (a) and 160 MPa (b) injection pressure and a range of in-cylinder pressures (ICP). Solid lines represent the residual fluid's penetration, and dotted lines the liquid jet's penetration. The lifetime of the residual fluid appears to be governed by the balance between kinetic and surface tension forces, which are primarily determined by the injection pressure and the fuel's physical properties. Higher injection pressures increase the kinematic energy of the injected fuel, and therefore lead to a shorter lifetime. Here the residual fluid is overtaken, and disintegrated, by the liquid jet within ≈30 μs for 40 MPa and less than 20 μs for 160 MPa injection pressure. The in-cylinder pressure has a negligible influence on the velocity and emergence of the residual fluid and liquid jets.

Badock et al. [12] did report the existence of this mushroom-like structure at non-evaporating conditions, without fully investigating its origin and temporal evolution, possibly dismissing it as a peculiarity resulting from their customised injector and working fluid.

The lifetime of the residual fluid appears to be governed by the balance between kinetic and surface tension forces, which are primarily determined by the injection pressure and the fuel's physical properties. Higher injection pressures increase the kinematic energy of the injected fuel, and therefore lead to a shorter lifetime. Fig. 12 shows the effect of the in-cylinder and injection pressures on the initial penetration of diesel fuel sprays. These measurements are based on individual ultra-high-speed videos recorded at 500 000 frames per second. The fuel was injected at 40 MPa and 160 MPa injection pressures into 4, 6 and 8 MPa in-cylinder pressures. The solid lines represent the residual fluid's penetration, and the dotted lines the liquid jet's penetration. From this chart we can estimate the lifetime of the residual fluid at ≈30 μs for 40 MPa and less than 20 μs for 160 MPa injection pressure. The in-cylinder pressure has a negligible influence on the velocity and emergence of the residual fluid and liquid jets.

4. Conclusions

In this study we presented microscopic images of diesel sprays at both atmospheric and diesel engine-like operating conditions. We investigated the primary atomisation of diesel, biodiesel and kerosene fuels in the near-nozzle region both at atmospheric and realistic engine conditions. Such high spatial and temporal resolutions allowed a detailed observation of the very emergence of fuel from the nozzle orifice. These observations indicated that the initial stage of fuel injection is more complex than the accepted linear temporal evolution.

As occasionally reported by other researchers at atmospheric conditions, we observed that the fluid that first exited the nozzle resembled mushroom-like structures, and that a microscopic ligament could be expelled ahead of the jet.

We captured the dynamics of this phenomenon at up to 5 million images per second using an ultra-fast framing camera fitted with a long-range microscope, and identified the mushroom-like structures as residual fluid trapped inside the nozzle orifices between injections. We found that the residual fluid had an internal vortex ring motion which resulted in a slipstream effect that propelled a microscopic ligament of liquid fuel ahead. We showed that this mechanism is not limited to laboratory setups, and that it occurs in the latest generation of injectors, with diesel fuels injected at engine-like conditions.

Our findings confirm that fuel can remain trapped in the injector holes after the end of injection. We could not measure the hydrocarbon content of the trapped vapourised fluid, but we observed that its density was lower than that of the liquid fuel, and higher than that of the in-cylinder gas. We conclude that high-fidelity numerical models should not assume in their initial conditions that the sac and orifices of fuel injectors are filled with liquid fuel or in-cylinder gas. Instead, our observations suggest that the nozzle holes be should be considered partially filled with a dense fluid.

Acknowledgements

This work was funded by BP International Ltd. and the UK's EPSRC [CASE studentship 07000437; Grant EP/K020528/1]. The authors are grateful to Ricardo UK for supplying equipment, and to the EPSRC Engineering Instrument Pool for the loan of instruments used for this study.

All data presented in this article [29] are openly available from the University of Brighton data archive at http://dx.doi.org/10/38n.

Appendix A. Supplementary material

Supplementary data associated with this article can be found, in the online version, at http://dx.doi.org/10.1016/j.fuel.2015.04.041.

References

[1] Dumouchel C. On the experimental investigation on primary atomization of liquid streams. Exp Fluids 2008;45(3):371–422. http://dx.doi.org/10.1007/s00348-008-0526-0.
[2] Eggers J, Villermaux E. Physics of liquid jets. Rep Prog Phys 2008;71(3):036601. http://dx.doi.org/10.1088/0034-4885/71/3/036601.
[3] Faeth GM, Hsiang LP, Wu PK. Structure and breakup properties of sprays. Int J Multiphase Flow 1995;21:99–127. http://dx.doi.org/10.1016/0301-9322(95)00059-7.
[4] Gorokhovski M, Herrmann M. Modeling primary atomization. Annu Rev Fluid Mech 2008;40(1):343–66. http://dx.doi.org/10.1146/annurev.fluid.40.111406.102200.
[5] Heimgärtner C, Leipertz A. Investigation of primary diesel spray breakup close to the nozzle of a common rail high pressure injection system. In: 8th ICLASS, Pasadena, USA, July 2000. <http://ilasseurope.org/publications/proceedings>.
[6] Hossainpour S, Binesh A. Investigation of fuel spray atomization in a DI heavy-duty diesel engine and comparison of various spray breakup models. Fuel 2009;88(5):799–805. http://dx.doi.org/10.1016/j.fuel.2008.10.036.
[7] Lefebvre A. Atomization and sprays. New York: Hemisphere Publishing; 1989.
[8] Liu Z, Im K-S, Wang Y, Fezzaa K, Harkay K, Sajaev V, Emery L, Wang J. Ultra-fast phase-contrast X-ray imaging of near-nozzle velocity field of high-speed diesel

fuel sprays. In: 22nd ILASS-Americas, Cincinnati, USA, May 2010. <http://ilass.org/2/ConferencePapers/ILASS2010-169.PDF>.
[9] Som S, Aggarwal SK. Effects of primary breakup modeling on spray and combustion characteristics of compression ignition engines. Combust Flame 2010;157(6):1179–93. http://dx.doi.org/10.1016/j.combustflame.2010.02.018.
[10] Sjberg H, Manneberg G, Cronhjort A. Long-working-distance microscope used for diesel injection spray imaging. Opt Eng 1996;35(12):3591–6. http://dx.doi.org/10.1117/1.601113.
[11] Lai M, Wang T, Xie X, Han J, Henein N, Schwarz E, et al. Microscopic characterization of diesel sprays at VCO nozzle exit. SAE Technical Paper 982542; 1998. http://dx.doi.org/10.4271/982542.
[12] Badock C, Wirth R, Fath A, Leipertz A. Investigation of cavitation in real size diesel injection nozzles. Int J Heat Fluid Flow 1999;20(5):538–44. http://dx.doi.org/10.1016/S0142-727X(99)00043-0.
[13] Bae C, Yu J, Kang J, Kong J, Lee K. Effect of nozzle geometry on the common-rail diesel spray. SAE Technical Paper 2002-01-1625; 2002. http://dx.doi.org/10.4271/2002-01-1625.
[14] McGuinness CD, Sagoo K, McLoskey D, Birch DJS. A new sub-nanosecond led at 280 nm: application to protein fluorescence. Meas Sci Technol 2004;15(11):L19. http://dx.doi.org/10.1088/0957-0233/15/11/L02.
[15] O'Hagan WJ, McKenna M, Sherrington DC, Rolinski OJ, Birch DJS. MHz LED source for nanosecond fluorescence sensing. Meas Sci Technol 2002;13(1):84. http://dx.doi.org/10.1088/0957-0233/13/1/311.
[16] Crua C, Shoba T, Heikal MR, Gold MR, Higham C. High-speed microscopic imaging of the initial stage of diesel spray formation and primary breakup. SAE Technical Paper 2010-01-2247; 2010. http://dx.doi.org/10.4271/2010-01-2247.
[17] Shoba T, Crua C, Heikal MR, Gold MR. Optical characterisation of diesel, rme and kerosene sprays by microscopic imaging. In: 24th ILASS-Europe, Estoril, Portugal, 5–7 Sep 2011. <http://ilasseurope.org/publications/proceedings/>.
[18] Crua C, de Sercey G, Heikal MR. Dropsizing of near-nozzle diesel and rme sprays by microscopic imaging. In: 12th ICLASS, Heidelberg, Germany, 2–6 Sep 2012. <http://ilasseurope.org/publications/proceedings/>.
[19] Crua C, de Sercey G, Gold M, Heikal M. Image-based analysis of evaporating diesel sprays in the near-nozzle region. In: 25th ILASS-Europe, Crete, Greece, 1–9 Sep 2013. <http://ilasseurope.org/publications/proceedings/>.
[20] Manin J, Bardi M, Pickett LM, Dahms RN, Oefelein JC. Microscopic investigation of the atomization and mixing processes of diesel sprays injected into high pressure and temperature environments. Fuel 2014;134:531–43. http://dx.doi.org/10.1016/j.fuel.2014.05.060.
[21] Crua C. Combustion processes in a diesel engine [Ph.D. thesis]. Brighton, UK: University of Brighton; 2002. <http://eprints.brighton.ac.uk/1161/>.
[22] Karimi K. Characterisation of multiple-injection diesel sprays at elevated pressures and temperatures [Ph.D. thesis]. Brighton, UK: University of Brighton; 2007. <http://eprints.brighton.ac.uk/3031/>.
[23] Reddemann A, Manuel, Mathieu F, Kneer R. Transmitted light microscopy for visualizing the turbulent primary breakup of a microscale liquid jet. Exp Fluids 2013;54(11):1–10. http://dx.doi.org/10.1007/s00348-013-1607-2.
[24] Settles GS. Schlieren and shadowgraph techniques. Experimental fluid mechanics. Berlin, Heidelberg: Springer; 2001. http://dx.doi.org/10.1007/978-3-642-56640-0.
[25] Roisman IV, Araneo L, Tropea C. Effect of ambient pressure on penetration of a diesel spray. Int J Multiphase Flow 2007;33(8):904–20. http://dx.doi.org/10.1016/j.ijmultiphaseflow.2007.01.004.
[26] Desantes JM, Payri R, García A, Manin J. Experimental study of biodiesel blends' effects on diesel injection processes. Energy Fuels 2009;23(6):3227–35. http://dx.doi.org/10.1021/ef801102w.
[27] Hiroyasu H, Arai M. Structure of fuel sprays in diesel engines. SAE Technical Paper 900475; 1990. http://dx.doi.org/10.4271/900475.
[28] Naber JD, Siebers DL. Effects of gas density and vaporization on penetration and dispersion of diesel sprays. SAE Technical Paper 960034; 1996. http://dx.doi.org/10.4271/960034.
[29] Crua C, Shoba T. Microscopic imaging of the initial stage of diesel spray formation. University of Brighton data archive, 2015. http://dx.doi.org/10/38n.